Efficient Full-Waveform Inversion via QR-Based Data Selection

Arnaud Mercier
Institute of Geophysics, ETH Zurich, Switzerland
Email: arnaud.mercier@eaps.ethz.ch

Christian Boehm
Mondaic AG, Switzerland

Hansruedi Maurer
Institute of Geophysics, ETH Zurich, Switzerland,

This manuscript is a non–peer-reviewed preprint submitted to EarthArXiv. The work has also been submitted for peer review to Geophysical Journal International.

Full-waveform inversion (FWI) is computationally intensive due to the large number of data points, forward simulations, and model parameters. However, realistic acquisition geometries often produce highly redundant linearized systems. In this work, we reformulate post-acquisition data selection as a matrix row-subset selection problem acting directly on the Jacobian of the linearized inverse problem. Using rank-revealing QR factorization, we introduce two complementary strategies: (i) row-wise selection to reduce the size of the linear system while preserving conditioning, and (ii) cost-aware selection to minimize the number of unique forward and adjoint simulations. In addition, we incorporate wavelet-based model compression derived from the Hessian diagonal to reduce the dimension of the update space. The methods are evaluated on synthetic elastic FWI experiments for crosshole and surface acquisition geometries. Row-wise QR selection consistently outperforms random subsampling and achieves accurate reconstructions using a fraction of the original data points. Cost-aware selection significantly reduces simulation cost with limited degradation of inversion quality. Model compression further decreases the number of active parameters, with compressibility strongly dependent on acquisition illumination. These results demonstrate that computational complexity in FWI can be controlled strategically by identifying the dominant bottleneck, memory, simulation cost, or model dimension, and applying the corresponding algebraic reduction mechanism. Although illustrated for seismic FWI, the proposed framework extends to inverse problems where the Gauss–Newton system is explicitly constructed or approximated, enabling algebraic manipulation of the Jacobian for data selection.

Contents

1 Introduction

Full-waveform inversion (FWI) has become a cornerstone technique for high-resolution seismic imaging, as it exploits the complete waveform information to infer quantitative subsurface models. By embedding accurate wave-propagation physics within an optimization framework, FWI can, in principle, resolve complex structures that are invisible to ray-based methods (Virieux et al. 2009). Despite these advantages, the practical deployment of FWI at scale remains limited by its computational cost.

Irrespective of the specific FWI formulation or numerical solver used, the costs arise from two dominant sources. First, repeated forward and adjoint wavefield simulations are required to compute gradients and sensitivity kernels in iterative optimization schemes. Second, linearized subproblems, typically least-squares systems involving large Jacobian matrices, incur substantial memory and linear algebra costs when the data volume is large. These limitations become particularly acute in three-dimensional, multiparameter, or high-frequency settings, where the size of the data and model space can be extremely large.

A key observation underlying this work is that realistic seismic surveys typically exhibit redundancies. Several studies have shown that only a small fraction of sources or measurements is sufficient to recover most of the information content of a full survey, indicating substantial redundancy in both the data and the associated sensitivity matrices (Maurer, Nuber, et al. 2017; Nuber et al. 2017). This observation is further supported by the success of randomized and compressive approaches to FWI, where accurate model updates can be obtained from randomly selected subsets of the data (Herrmann et al. 2013; Li et al. 2012). As a consequence, solving the full linearized problem using all available data is often unnecessary. These are good news, because realistically-sized seismic data sets (e.g., from hydrocarbon exploration surveys) requires significant compute resources.

Several strategies have been proposed to mitigate this cost by reducing the amount of data used during inversion. Random subsampling and dynamic mini-batching reduce computational efforts, but offer limited control over conditioning and are sensitive to stochastic noise (Li et al. 2012; Herrmann et al. 2013; Herwaarden et al. 2020). Source encoding and blending techniques decrease the number of wavefield simulations by combining multiple sources into encoded experiments, but they do not construct explicit data subsets and instead mix sensitivities from different sources, possibly losing information due to interference (Castellanos et al. 2015; Krebs et al. 2009).

Alternative approaches, based on optimized experimental design (OED), formulate data selection using tools from linear(ized) inversion theory, but they are typically aimed at pre-acquisition survey design and rely on eigenvalue- or singular-value-based metrics that can be difficult to scale to large problems (Curtis 1999; Maurer, Nuber, et al. 2017; Nuber et al. 2017; Krampe et al. 2021). Heuristic criteria based on illumination or wavenumber coverage, while intuitive, lack robustness and generality in multiparameter FWI. For example, Abdellaziz et al. 2025 developed a formal OED criteria based on uniform wavenumber sampling, but this method is limited to a specific target in the model space.

These limitations motivate a post-acquisition data selection strategy aimed at reducing the size of the linearized inverse problem. Rather than redesigning the survey geometry prior to data collection, we consider selecting a subset of measurements from an already acquired data set. For example, in large-scale 3D seismic surveys, typically huge amounts of data have to be acquired for obtaining un-aliased subsurface images. However, such data sets are usually not tractable with FWI techniques. When FWI is employed for obtaining a reliable velocity model that can be subsequently used for reverse time migration, it is mostly sufficient to work with a suitably chosen data subset. Within a linearized inversion framework, this amounts to choosing a subset of equations that preserves the essential structure and stability of the full system.

From a linear algebra perspective, this formulation corresponds to a matrix row-subset selection problem: identifying a subset of rows that preserves the conditioning of the linearized inverse problem, while reducing computational cost. For that purpose, rank-revealing QR factorizations provide an effective algebraic tool, and they have been extensively studied in the context of column and row subset selection (Businger et al. 1965; Gu et al. 1996). More specifically, QR factorization with column pivoting (CPQR) has been shown to produce near–maximum-volume submatrices with attractive conditioning guarantees (Drmač et al. 2016).

Building on these developments, QR-based subset selection has been successfully applied in data-driven sparse sensor placement, where a low-rank basis of representative states or sensitivities is constructed and CPQR is used to select informative measurement locations (Manohar et al. 2018; Clark et al. 2020). For large-scale problems, randomized and blocked variants of rank-revealing QR factorizations enable such selections to be computed efficiently (Halko et al. 2011; Murray et al. 2023). Furthermore, QR-based algorithms have been used for sensor placement in the context of linear PDEs and seismic travel time tomography (Eswar et al. 2024).

In this work, we extend these ideas to the specific structure and computational constraints of seismic FWI. While QR-based subset selection has been widely studied in numerical linear algebra and sensor placement problems, these approaches do not account for the computational structure of FWI, where sensitivities are generated through expensive forward and adjoint wavefield simulations and where the Jacobian exhibits a natural block structure associated with source–receiver pairs.

To address these constraints, we introduce two QR-based data selection strategies targeting different computational bottlenecks: a row-wise CPQR approach that prioritizes memory reduction by selecting individual rows, and a cost-aware approach that minimizes the number of unique forward and adjoint simulations required. The choice between these strategies depends on whether the inversion is primarily memory-bound or compute-bound.

The remainder of the paper is organized as follows. Section 2 introduces the inverse problem formulation and the framework that defines the Jacobian-based linearized systems considered in this work. Section 3 presents in detail the two QR-based data selection strategies. In Section 4, the developed methods are tested in numerical experiments while Section 5 discusses the results, implications and limits.

Although the numerical results presented in this paper focus on seismic FWI, the proposed framework is not specific to seismic imaging. It applies to a broader class of gradient-based inverse problems, in which sensitivities or Jacobians are available, including other wave-based imaging modalities. By reframing data reduction as a row-selection process driven by computational constraints, this work provides a flexible, post-acquisition alternative to existing subsampling and design strategies for large-scale inverse problems.

2 Linearized inverse problem and data structure

Nonlinear inverse problem

We consider inverse problems in which a set of model parameters $\mathbf{m} \in \mathbb{R}^m$ is inferred from observed data $\mathbf{d}_{\text{obs}} \in \mathbb{C}^d$ through a forward operator $\mathcal{F}$ that maps model parameters to predicted data,

$$\mathbf{d}_{\text{pred}} = \mathcal{F}(\mathbf{m}). \tag{1}$$

A common inverse problem formulation consists in finding $\mathbf{m}$ that minimizes the least-squares misfit between observed and predicted data,

$$\chi(\mathbf{m}) = \frac{1}{2}\,\|\mathbf{d}_{\text{obs}} - \mathcal{F}(\mathbf{m})\|_2^2\,, \tag{2}$$

In FWI and many applications of interest, the number of model parameters is very large, often exceeding 10^4–10^6. In such high-dimensional settings, fully probabilistic or sampling-based approaches quickly become computationally prohibitive, and practical solutions are typically sought using deterministic, iterative optimization methods starting from an initial model $\mathbf{m}_0$ (Tarantola 2005; Virieux et al. 2009).

Linearization and sensitivity matrix

To compute model updates within this iterative framework, the misfit function is locally approximated around the current model estimate. Expanding the least-squares misfit $\chi(\mathbf{m})$ in a Taylor series around $\mathbf{m}_k$ yields the quadratic approximation

$$\chi(\mathbf{m}_k + \delta\mathbf{m}) \;\approx\; \chi(\mathbf{m}_k) + \nabla\chi(\mathbf{m}_k)^\top \delta\mathbf{m} + \frac{1}{2}\,\delta\mathbf{m}^\top \mathbf{H}_k\,\delta\mathbf{m}, \tag{3}$$

where $\nabla\chi(\mathbf{m}_k)$ and $\mathbf{H}_k$ denote the gradient and Hessian of the misfit with respect to the model parameters.

Minimizing the quadratic approximation with respect to $\delta \mathbf{m}$ leads to the optimality condition

$$\mathbf{H}_k \delta \mathbf{m} = -\nabla \chi(\mathbf{m}_k). \tag{4}$$

For a least-squares misfit, the dependence of $\chi(\mathbf{m})$ on the model parameters enters solely through the forward operator $\mathcal{F}(\mathbf{m})$. As a consequence, the gradient and Hessian of the misfit can be expressed in terms of the Jacobian matrix $\mathbf{J}_k = \partial \mathcal{F} / \partial \mathbf{m}|_{\mathbf{m}_k}$. In the Gauss–Newton approximation, which is here chosen for its attractive convergence properties, second-order derivatives of the forward operator are neglected, and the Hessian is approximated by $\mathbf{H}_k \approx \mathbf{J}_k^\top \mathbf{J}_k$. This yield the following normal equations, where $\mathbf{L}^\top \mathbf{L}$ is a regularization (damping/smoothing) term with amplitude λ.

$$\left[\mathbf{J}_k^\top \mathbf{J}_k + \lambda^2 \mathbf{L}^\top \mathbf{L}\right] \delta \mathbf{m} = \mathbf{J}_k^\top \delta \mathbf{d}_k, \qquad \delta \mathbf{d}_k = \mathbf{d}_{\text{obs}} - \mathcal{F}(\mathbf{m}_k) \tag{5}$$

This formulation emphasizes the central role of the Jacobian matrix in Gauss–Newton optimization scheme: it governs both the gradient and the approximate curvature of the misfit function and dominates the conditioning and computational cost of the linearized system. Consequently, selecting informative subsets of rows of $\mathbf{J}_k$ directly impacts the efficiency and performance of the inversion and constitutes the focus of the data selection strategies developed in this work.

Jacobian structure and indexing

The proposed data-selection framework targets inverse problems in which the data can be decomposed into a set of distinct measurements, each associated with a single row of the Jacobian matrix. In this setting, the Jacobian admits a row-wise representation in which individual measurements define separate linearized equations, thereby defining a natural level of resolution at which data selection can be performed. In this work, we focus on frequency-domain FWI as a representative instance of this class of problems.

The Jacobian matrix in FWI is constructed using the adjoint-state method (Fichtner 2010). In our implementation, forward and adjoint wavefields are simulated in the time domain, while frequency-domain quantities are accumulated on the fly through discrete Fourier transforms at the frequencies of interest. This avoids storing the full time history and provides direct access to the sensitivities required to assemble the Jacobian from the interaction of forward and adjoint fields. To compute the sensitivities in the Jacobian matrix, we make use of the explicit expressions described in Zhou et al. 2009. Consequently, a forward simulation has to be carried out for every source and receiver position.

Each data point corresponds to a single row of the Jacobian. In the frequency-domain formulation adopted here Pratt et al. 1998, a row is associated with a specific source–receiver–frequency triplet (s, r, ω), while the columns represent model parameters (m). Rows may optionally be grouped into blocks corresponding to a fixed source–receiver pair (s, r) across all selected frequencies, as illustrated in Figure 1. This block structure is convenient when introducing cost-aware or source-dependent row-selection strategies. The total size of the Jacobian is governed by the number of source–receiver–frequency triplet d and the number of discretized model parameters m. For realistic acquisition geometries involving hundreds of sources and receivers and multiple frequencies, this typically results in data spaces that exceed the model dimension by one to several orders of magnitude, leading to strongly overdetermined systems (Virieux et al. 2009; Fichtner 2010).

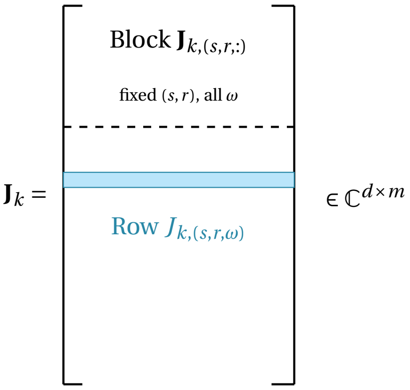

Figure 1: Schematic of the Jacobian matrix. Each row corresponds to a linearized data equation, indexed by a source-receiver-frequency triplet (s,r,ω). In addition to individual rows, the Jacobian admits a natural block structure where $\mathbf{J}_{k,(s,r,:)}$ groups all frequencies for a fixed (s,r).

Post-acquisition data selection

We consider a post-acquisition setting, in which the data have already been collected and the acquisition geometry is fixed. Within the Gauss–Newton framework defined in equation 5, post-acquisition data selection corresponds to restricting the set of linearized equations by selecting a subset of rows (or blocks) of the Jacobian matrix. This operation reduces the number of data equations while leaving the dimension of the model update unchanged.

Introducing a selection operator $\mathbf{S}$ that extracts a subset of rows, equation 5 becomes,

$$\left[(\mathbf{S}\mathbf{J}_k)^\top(\mathbf{S}\mathbf{J}_k)+\lambda^2\mathbf{L}^\top\mathbf{L}\right]\delta\mathbf{m}=(\mathbf{S}\mathbf{J}_k)^\top(\mathbf{S}\delta\mathbf{d}_k). \tag{6}$$

The objective of data selection is to reduce memory usage and computational cost, while preserving the essential information content and conditioning of the original Gauss-Newton system. This formulation defines a clear interface for algorithmic selection strategies: given a Jacobian matrix, or a matrix-free representation thereof, the task is to identify informative subsets of rows or blocks. The QR-based selection methods introduced in the next section operate directly on this formulation.

Model space compression

In addition to data selection, we introduce model-space compression as a complementary strategy to reduce the cost of solving the Gauss–Newton system. Rather than operating directly in the physical parameter domain, we transform the model parameters into a basis, in which the Jacobian exhibits a sparse representation. This enables the identification and retention of the most informative components while discarding weakly contributing parameters with minimal loss of accuracy. In practice, we apply a discrete wavelet transform to the model parameters for each Jacobian row and rank the resulting coefficients using the diagonal of the approximate Gauss–Newton Hessian ($\mathbf{J}^\top\mathbf{J}$) as a measure of parameter sensitivity. Coefficients associated with low sensitivity are removed, leading to a reduced-dimensional update space. This strategy is particularly well suited to seismic inversion, where spatial correlations and multiscale structure allow for efficient representation in a wavelet basis (Xu et al. 2020; Mercier et al. 2025).

Let $\delta\mathbf{m} = \mathbf{P}\,\delta\tilde{\mathbf{m}}$, where $\delta\tilde{\mathbf{m}}$ denotes the retained wavelet coefficients in the compressed model space. The Gauss–Newton system is therefore solved for $\delta\tilde{\mathbf{m}}$, yielding

$$\left[(\mathbf{S}\mathbf{J}_k\mathbf{P})^\top(\mathbf{S}\mathbf{J}_k\mathbf{P}) + \lambda^2\tilde{\mathbf{L}}^\top\tilde{\mathbf{L}}\right]\delta\tilde{\mathbf{m}} = (\mathbf{S}\mathbf{J}_k\mathbf{P})^\top(\mathbf{S}\delta\mathbf{d}_k). \tag{7}$$

The computational workflow proceeds in two stages: data selection is performed first through $\mathbf{S}$, reducing the linearized system in data space, and model compression is introduced subsequently through $\mathbf{P}$ when solving the Gauss–Newton system.

The unknown of the reduced system is thus the compressed update $\delta\tilde{\mathbf{m}}$. Once computed, the update in physical parameter space is recovered through the inverse transformation

$$\delta\mathbf{m} = \mathbf{P}\,\delta\tilde{\mathbf{m}}. \tag{8}$$

The regularisation term $\lambda^2\tilde{\mathbf{L}}^\top\tilde{\mathbf{L}}$ is applied directly in the compressed domain. Because the wavelet truncation removes weakly sensitive and high-frequency components, the compression itself acts as an implicit regularisation mechanism. As a consequence, the required strength of classical Tikhonov-type regularisation is typically reduced.

3 Methodology

Following the formulation of post-acquisition data selection defined in section 2, we design a purely algebraic method that operates directly on the Jacobian, without modifying the forward operator, the misfit function, or the optimization scheme. To this end, we adapt column pivoting QR factorization (CPQR) to the specific structure and constraints of full-waveform inversion (Eswar et al. 2024). Two complementary selection strategies are introduced. The first performs row-wise selection of the Jacobian and primarily targets memory and linear-algebra costs. The second exploits the block structure governed by source–receiver pairs and incorporates a cost model to explicitly control the number of numerical forward simulations (one simulation for each source and receiver position).

The CPQR factorization is performed once prior to the inversion, using the full Jacobian evaluated at a reference model. The resulting subset is then kept fixed throughout all subsequent Gauss–Newton iterations. In this study, the Jacobian is evaluated at the true model in order to isolate and assess the intrinsic performance of the proposed method. In practice, however, OED is performed using the initial model, under the Gauss–Newton assumption that the linearization is locally valid. Previous work has shown that the resulting designs are relatively insensitive to this choice (**Maurer2017**; **Krampe2021**; **Nuber2017**).

3.1 Row-wise QR selection

CPQR provides an effective mechanism for ordering the columns of a matrix so that the leading columns form a well-conditioned basis for the column space (Golub et al. 1996). Applied to the transposed Jacobian $\mathbf{J}^\top$, the resulting pivot order induces a ranking of the rows of $\mathbf{J}$, i.e., of the linearized equations, based on linear independence and numerical conditioning.

Because the Jacobian arising in FWI is typically too large to be factorized explicitly, we first construct a low-dimensional representation with operator $\boldsymbol{\Omega}$, that preserves its dominant column-space structure. This is typically achieved through a randomized projection onto a reduced model subspace with oversampling o (Duersch et al. 2017; Murray et al. 2023). However, sensitivities in the model space can be very uneven with parts of the model being poorly illuminated. We therefore suggest a compression scheme based on a hierarchical transform, namely a wavelet transform (Xu et al. 2020; Mercier et al. 2025) similar to the one introduced in Section 2. This approach effectively balances the representation of different model regions while preserving the essential features of the Jacobian. The compression used prior to the QR factorization acts in the model space, that is, on the column space of $\mathbf{J}$. This preserves the row-space structure and therefore the interpretability of the resulting pivot sequence in terms of selecting rows of the original Jacobian. Its sole purpose is to construct a computationally tractable surrogate matrix $\mathbf{B}$ for the CPQR step; it does not modify the inversion itself and is entirely decoupled from the model-space compression operator $\mathbf{P}$ introduced in the Gauss–Newton formulation. The compression ratio for the QR step is chosen according to the targeted data-space reduction and is independent of the compression ratio used for operator $\mathbf{P}$ in the inversion. Applying CPQR to $\mathbf{B}$ produces a pivot ordering that maps to rows of the full Jacobian (Gu et al. 1996).

Selecting rows according to this pivot order yields a reduced system that remains well conditioned and representative of the full Gauss-Newton problem. This row-wise selection strategy is deterministic once the low-dimensional representation is fixed and is particularly effective when memory usage or the solution of the Gauss–Newton system dominates the computational cost. Algorithm 1 summarizes this QR-inspired row selection procedure.

Algorithm 1 QR-inspired row selection on a compressed Jacobian

```
Require: Jacobian matrix $\mathbf{J} \in \mathbb{C}^{d\times m}$; Number of rows to select $T$; oversampling $o$.
Ensure: $\mathbf{S}$ selected rows of $\mathbf{J}$ (in pivot order).
1: Set $p \leftarrow \min(T + o, m)$.
2: Define a compression operator $\mathbf{\Omega} \in \mathbb{C}^{m\times p}$.
3: Build a compressed matrix $\mathbf{B} \leftarrow \mathbf{\Omega}^\top \mathbf{J}^\top \in \mathbb{C}^{p\times d}$.
4: CPQR on $\mathbf{B}$ to obtain a pivot order over its $d$ columns.
5: Return Selection operator $\mathbf{S}$ corresponding to the first $T$ pivots.
```

3.2 Cost-aware QR Selection

While row-wise selection effectively reduces the size of the linearized system, it does not explicitly account for the computational cost associated with generating individual rows of the Jacobian. In waveform-based inversions, this cost is dominated by the numerical wavefield simulations, which are naturally shared by groups of rows corresponding to the same source-receiver pair.

To account for this structure, we introduce a cost-aware selection strategy that operates on blocks of rows associated with fixed source-receiver pairs but including all frequencies ω as displayed in Figure 1. This grouping represents the smallest granularity at which the number of unique forward and adjoint simulations can be controlled explicitly. Defining blocks in this way preserves flexibility in data reduction, while allowing a direct control of computational cost. The strategy therefore balances information gain and simulation effort without imposing unnecessary structural constraints.

The procedure is inspired by Gram-Schmidt QR with pivoting, but it is modified to operate at the block level and to include a user-defined cost model. At each iteration t, each unselected candidate block g is scored using the residual column energy of this compressed representation (e_j), where columns correspond to rows of the original Jacobian. Cost-awareness is introduced by penalizing blocks that activate previously unused sources or receivers, with factors c_{src} and c_{rec}, thereby avoiding activating additional simulations. At each iteration, the block maximizing the energy-to-cost ratio is selected, and its contribution is removed from the compressed matrix $\mathbf{B}$ through a deflation step (orthogonal projection), ensuring that subsequent selections prioritize complementary information. The procedure returns an ordered list of blocks $\mathbf{S}$ that balances information content and simulation cost. Algorithm 2 details this block selection procedure.

In contrast to standard CPQR routines, this approach needs to perform a manual deflation step, corresponding to matrix-matrix multiplications, to update the residual matrix after each block selection. Furthermore, the pivoting is implemented in a greedy outer loop (Line 4 and 5 of Algorithm 1). The CPQR that are computed in each iteration of the outer loop are of low computational cost because they operate on the chosen block of rows. Nonetheless, the cost-aware approach is computationally less efficient than the row-wise QR factorization used in Section 3.1. In contrast to standard CPQR implementations based on optimized BLAS-3 routines used for row selection, the need to access individual pivots at each iteration to incorporate cost penalties precludes the use of off-the-shelf algorithms and requires a custom implementation with explicit residual updates.

Algorithm 2 Cost-aware selection on a compressed Jacobian

```
Require: Data matrix $\mathbf{J} \in \mathbb{C}^{d\times m}$; penalties $c_{\text{src}}, c_{\text{rec}} \geq 0$; number of desired blocks $T$.
Ensure: Ordered selected blocks $\mathbf{S}$.
Build a compressed matrix $\mathbf{B} = \mathbf{\Omega}^\top \mathbf{J}^\top \in \mathbb{C}^{p\times d}$
Initialize residual energies $e_j \leftarrow \|\mathbf{B}_{:,j}\|_2^2$ for $j = 1,\dots,d$
$\mathcal{A}_{\text{src}} \leftarrow \emptyset$, $\mathcal{A}_{\text{rec}} \leftarrow \emptyset$, $\mathbf{S} \leftarrow \emptyset$
for $t = 1,\dots,T$ do:
    for each unselected block $g$ do:
        $\text{score}(g) = \dfrac{\sum_{j\in g} e_j}{\varepsilon + c_{\text{src}}\mathbb{1}[\text{new src}] + c_{\text{rec}}\mathbb{1}[\text{new rec}]}$
    end for
    $g^\star = \arg\max_g \text{score}(g)$
    $\mathbf{S} \leftarrow \mathbf{S} \cup \{g^\star\}$; update $\mathcal{A}_{\text{src}}, \mathcal{A}_{\text{rec}}$
    Deflate $\mathbf{B}$ using columns $j \in g^\star$; update $e_j \leftarrow \|\mathbf{B}_{:,j}\|_2^2$
end for
Return S
```

3.3 Summary of QR Selection Strategies

Figure 2 provides a schematic overview of the proposed selection workflow. Starting from the full Jacobian, a model-space reduction yields a compact core matrix that captures the essential row-space structure of the linearized problem. From this representation, two selection paths are available: row-wise selection and cost-aware selection.

Both strategies result in explicit selection operators **S** that can be applied directly within the Gauss-Newton framework described in Section 2. The choice between them depends on the dominant computational bottleneck of the inversion; memory and linear algebra costs versus the cost of forward and adjoint simulations. In both cases, the optimization scheme remains unchanged.

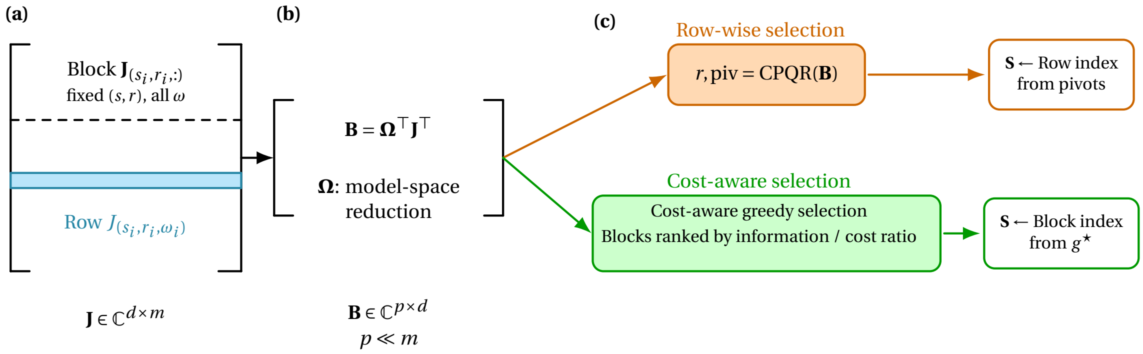

Figure 2: (a) Jacobian **J** with a block $\mathbf{J}_{s,r,:}$ (dashed separation) and single row $J_{s,r,\omega}$ (blue strip); (b) Model space reduction of **J** to reduce the m dimension to p such that **B** is representative of $\mathbf{J}^\top$ but with dimension $p \times d$. (c) From the **B** matrix there are 2 possible paths: (i) Row selection via CPQR to get row indices; (ii) cost-aware selection on blocks via QR inspired Gram-Schmidt to get block indices.

4 Numerical tests

We assess the proposed data-selection strategies on two synthetic elastic full-waveform inversion scenarios: a crosshole and a surface acquisition geometry (Figures 3 and 4). In both cases, the true models consist of smooth background velocities perturbed by localized low- and high-velocity anomalies. For the crosshole configuration, 20 sources and 20 receivers are positioned in opposing boreholes. The surface configuration comprises a linear surface spread and includes an additional velocity gradient with depth to promote diving waves. In both geometries, density is not inverted independently, but derived from the P-wave velocity using the Gardner relation, ensuring internal consistency between elastic parameters.

Forward modelling is performed in the time domain using a Ricker wavelet with a central frequency of 125 Hz, while the frequency domain output is accumulated on-the-fly (Afanasiev et al. 2019; Witte et al. 2019). The inversion is carried out in the frequency domain following the Gauss–Newton formulation described in Section 2, implemented with six discrete frequencies: 50, 90, 125, 150, 200, and 250 Hz. For the crosshole geometry, all frequencies are inverted simultaneously, as the acquisition provides sufficient illumination to avoid severe cycle-skipping. In contrast, for the surface geometry a simple frequency continuation strategy is adopted: the inversion is initialized with the three lowest frequencies (50–125 Hz), and the higher frequencies are introduced after 4 iterations. This schedule mitigates cycle-skipping effects associated with poorer illumination and stronger nonlinearity.

A constant damping term is applied in both geometries to stabilize the Gauss–Newton updates. The damping parameter is kept fixed across all subsequent experiments to ensure that differences in inversion performance arise solely from data-selection strategies and not from retuning of regularization.

As a reference, we first invert the comprehensive surveys comprising 4800 data points (i.e., all source–receiver–frequency triplets). The corresponding misfit evolutions and final inverted models are shown in Figures 5 and 6. These results serve as benchmarks for all reduced-data experiments. Although the reconstruction of V_P remains more challenging than that of V_S, both geometries yield satisfactory models that capture the main structural features of the true models. The crosshole geometry exhibits superior resolution and convergence behaviour, which is consistent with its more uniform illumination. The surface configuration is intrinsically more difficult, reflecting limited angular coverage and depth-dependent sensitivity.

These comprehensive inversions provide a stable and physically plausible baseline against which the impact of data-selection strategies can be quantified in the following sections.

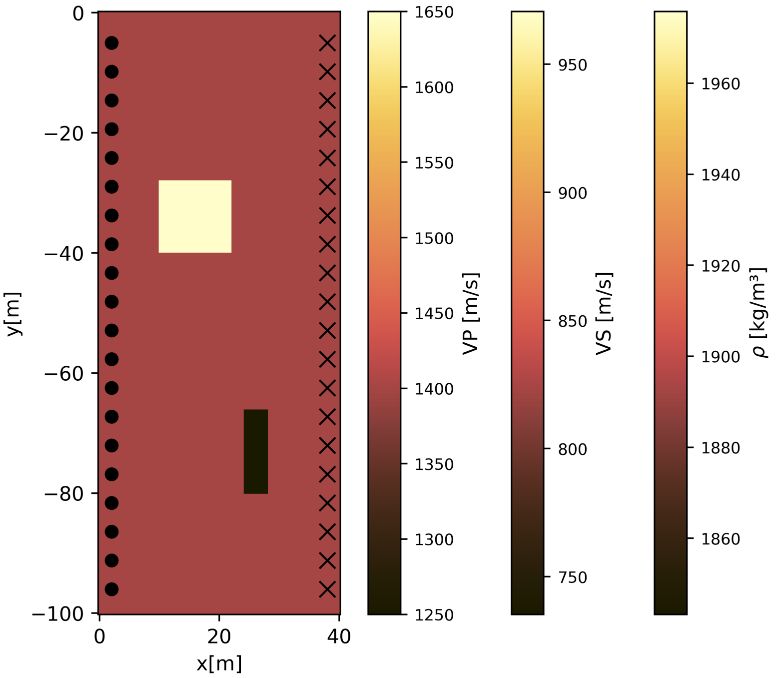

Figure 3: True models used for the crosshole numerical tests.

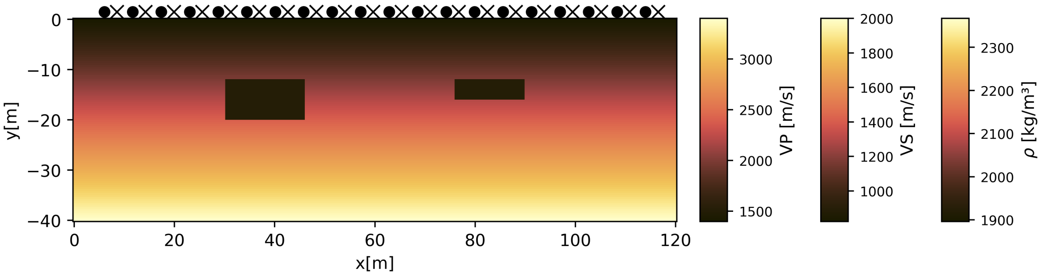

Figure 4: True models used for the surface numerical tests.

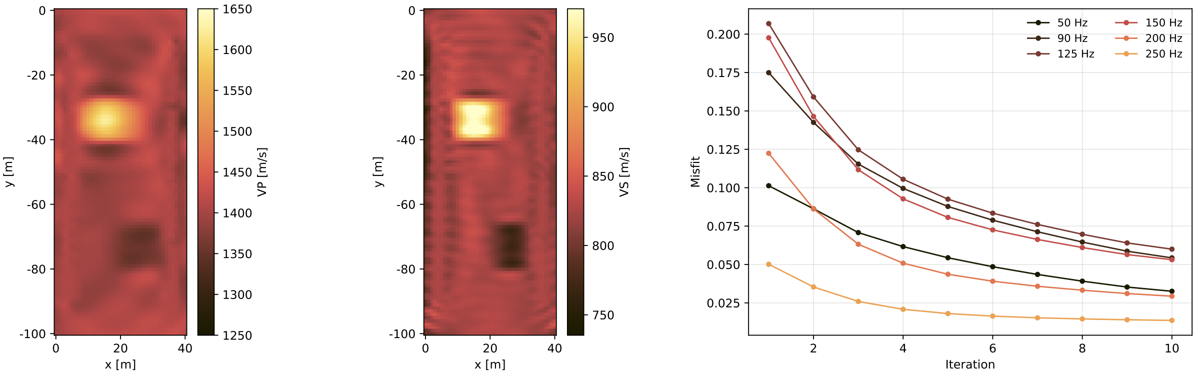

Figure 5: Inverted velocity models (V_P and V_S) using the comprehensive survey (4800 data points) for the crosshole geometry. The misfit for each frequency used is shown across the iterations.

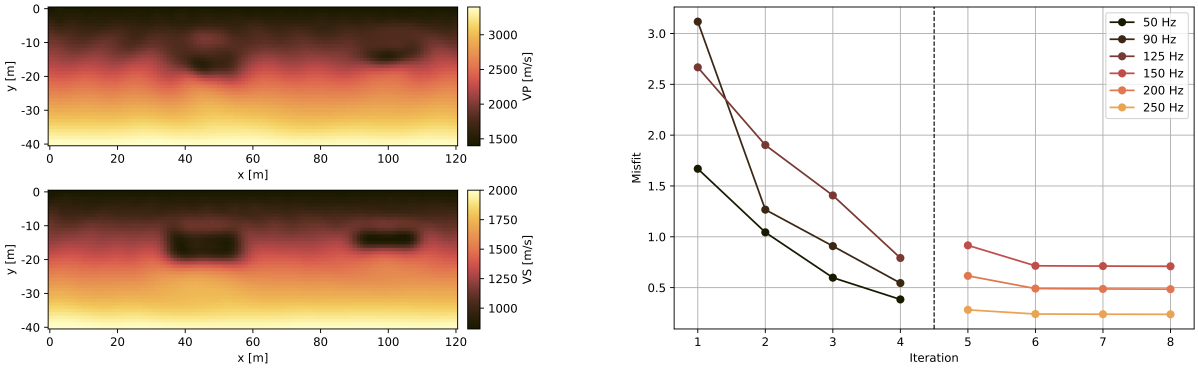

Figure 6: Inverted velocity models (V_P and V_S) using the comprehensive survey (4800 data points) for the surface geometry. A simple frequency schedule is used in order to mitigate cycle skipping issues. The misfit for each frequency are shown across iterations.

4.1 Row-wise QR selection

To quantitatively benchmark the row-wise QR selection strategy, described in Section 3.1, we compare its performance against random data selection for varying numbers of selected data points. For each fraction of retained data, we perform an inversion using the QR-selected rows and, in parallel, 20 independent inversions using randomly selected subsets containing the same number of rows. From these inversions, we compute three metrics: (i) the total misfit summed over all events, (ii) the L_2-norm difference between the inverted V_P model and the comprehensive-survey inverted V_P model, and (iii) the corresponding L_2-norm difference for V_S. In the resulting figures for both acquisition geometries, the dashed line represents the reference obtained with the comprehensive survey, while the shaded area indicates the variability across the 20 random realizations.

For the crosshole geometry, the QR-based selection consistently outperforms random selection across all metrics. The normalized misfit and the L_2-norm differences for V_P are systematically lower for QR than for random subsets at equal data fractions. For V_S, the difference between QR and random selection becomes small at higher fractions of retained data points. We interpret this behaviour as a consequence of the favourable illumination provided by the crosshole configuration. In this regime, even relatively small subsets of data points already yield a high-quality reconstruction of V_S, such that both random and QR selections converge toward similar solutions. In contrast, the reconstruction of V_P remains more sensitive to the choice of data points, and QR-based selection retains a clear advantage.

For the surface geometry, QR selection also outperforms random selection; however, this superiority becomes apparent only beyond approximately 12.5% of retained data points. Below this threshold, the inversion fails to converge to a meaningful solution and both V_P and V_S are poorly reconstructed. In this strongly underdetermined regime, the specific choice of data points has limited impact, because the inversion itself is ineffective. Once a sufficient fraction of data points is included, QR selection consistently yields lower misfits and smaller model differences than random selection, highlighting its ability to identify more informative subsets in a less favourably illuminated setting.

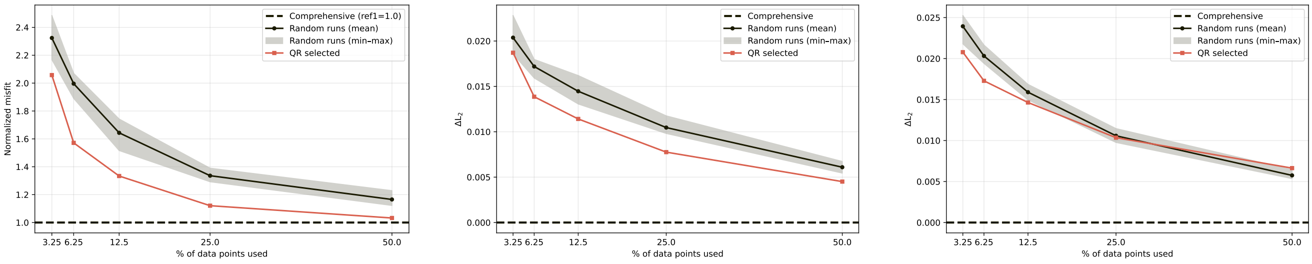

(a) **(b)** **(c)**

Figure 7: Comparison of inversion results for the crosshole geometry obtained with QR-based and random data selection: (a) normalized misfit; (b-c) L_2-norm differences relative to the comprehensive inverted V_P and V_S models. For the random runs, the solid lines represent the mean, and the shaded area represents the range (minimum–maximum) over 20 realizations.

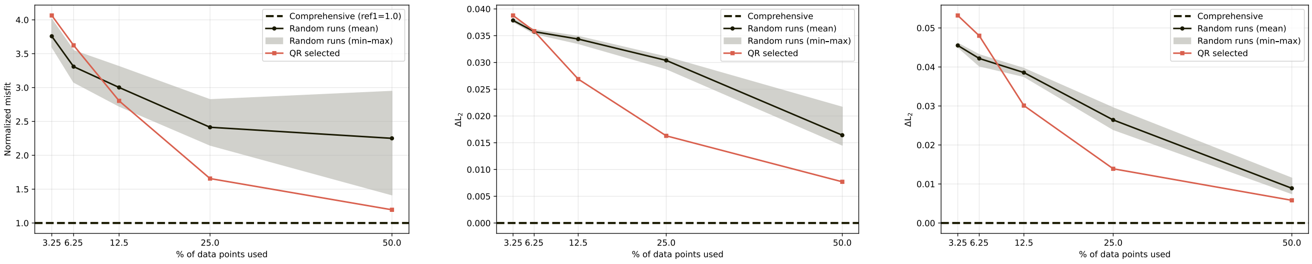

(a) **(b)** **(c)**

Figure 8: Comparison of inversion results for the surface geometry obtained with QR-based and random data selection: (a) normalized misfit; (b-c) L_2-norm differences relative to the comprehensive inverted V_P and V_S models. For the random runs, the solid lines represent the mean, and the shaded area represents the range (minimum–maximum) over 20 realizations.

The corresponding inverted models for different fractions of retained data points are shown in Figures 9 and 10, where they are compared to the comprehensive-survey results. For clarity, we display models starting from 50% of the data points, as this level already provides a good reconstruction and small differences relative to the reference solution. Qualitatively, for the crosshole geometry, satisfactory model reconstruction is achieved with as little as 12.5% of the data points. For the surface geometry, approximately 25% of the data points are required to reach a comparable level of reconstruction. This difference is consistent with the poorer illumination and stronger nonlinearity inherent to the surface acquisition configuration. As a reference, the inversion results for the mean random selection are shown in Section A.1.

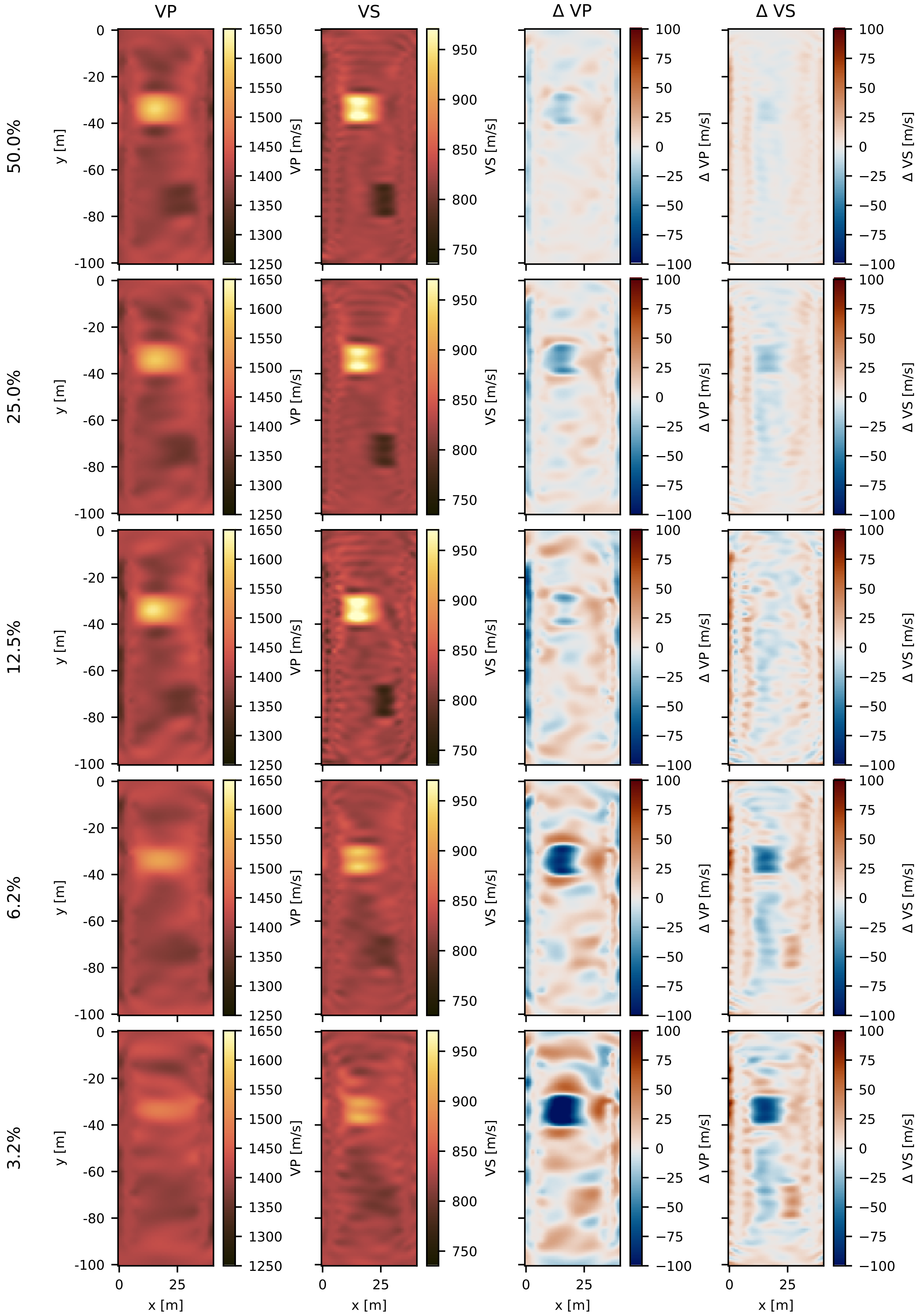

Figure 9: Inverted models of the crosshole geometry for different number of data points accompanied by their differences with respect to the inverted models with the comprehensive survey. Inversion results with 50% of the data already provides a very close approximation to the inversion results with the comprehensive dataset, as depicted by the minimal differences observed in the corresponding difference plot. For reference to the comprehensive survey results, see Figure 5.

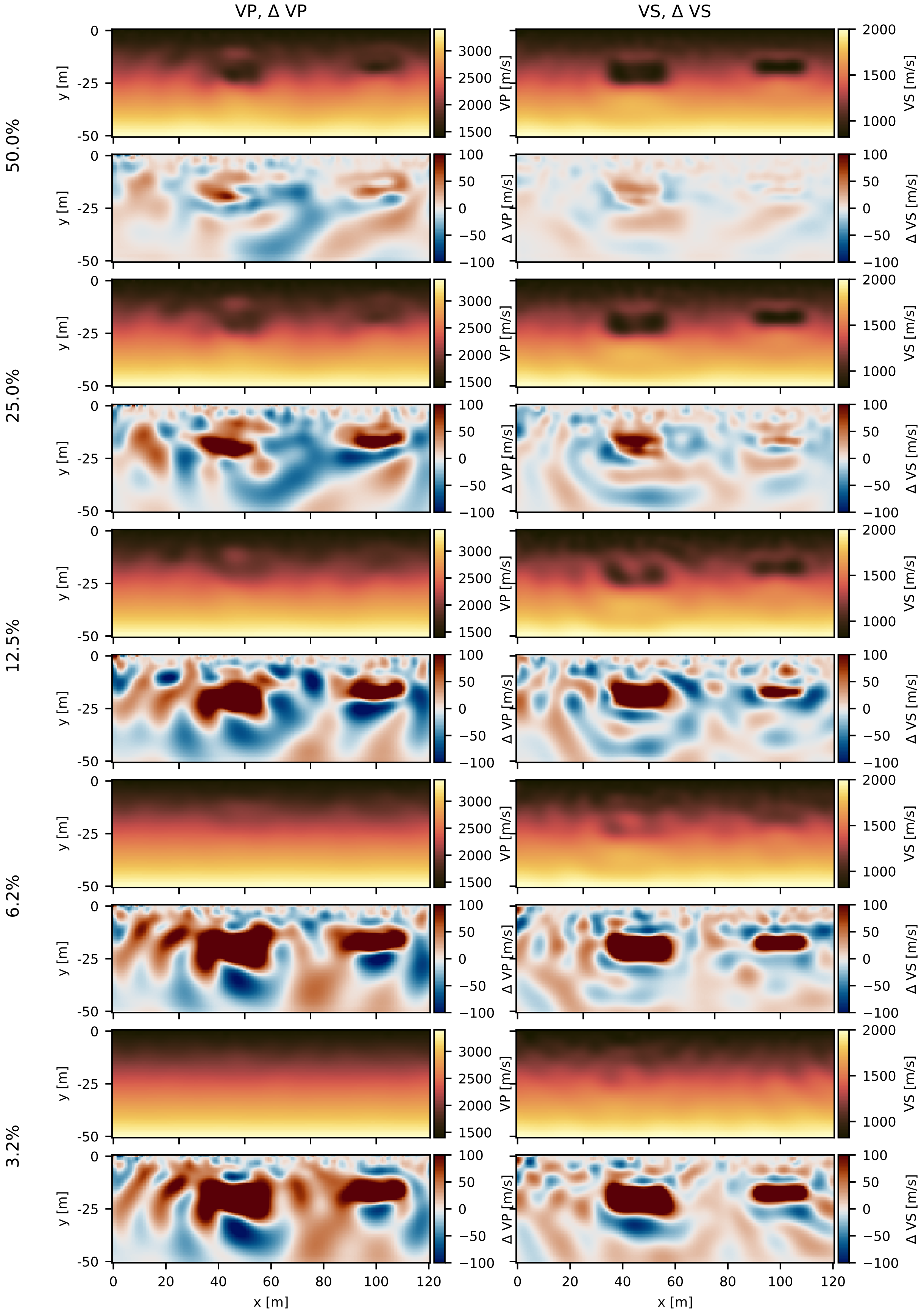

Figure 10: Inverted models of the surface geometry for different number of data points accompanied by their differences with respect to the inverted models with the comprehensive survey. Inversion results with 50% of the data already provides a good approximation to the inversion results with the comprehensive dataset, as depicted by the minimal differences observed in the corresponding difference plot. For reference to the comprehensive survey results, see Figure 6.

The previous results raise the practical question of how to determine an appropriate number of data points without performing multiple inversions for different subset sizes. To address this, we analyze the evolution of the sum of the diagonal entries of the approximate Hessian, $\mathbf{H} = \mathbf{J}^\top \mathbf{J}$, as a function of the number of selected data points for both geometries (Figure 11a). Since the Jacobian of the selected data points is already available, evaluating this quantity does not introduce significant additional computational costs.

Because the selection operates on the compressed matrix $\mathbf{B} = \boldsymbol{\Omega}^\top \mathbf{J}^\top$, we approximate the Hessian diagonal using the CPQR factors of $\mathbf{B}$. Specifically, with $\mathbf{B} = \mathbf{QR}$, we compute

$$\operatorname{diag}(\mathbf{H}) = \operatorname{diag}(\mathbf{J}^\top \mathbf{J}) \approx \operatorname{diag}(\mathbf{B}^\top \mathbf{B}) = \operatorname{diag}(\mathbf{R}^\top \mathbf{Q}^\top \mathbf{QR}) = \operatorname{diag}(\mathbf{R}^\top \mathbf{R}), \tag{9}$$

where orthogonality of $\mathbf{Q}$ has been used. The sum of these diagonal entries provides a scalar proxy for the accumulated curvature information captured by the selected data points.

Visual inspection of Figure 11a seems to indicate a rather continuous increase of the trace sum of the approximate Hessian. To better identify changes in this quantity, we additionally compute its discrete derivative with respect to the number of selected data points (Figure 11b). For both geometries, the derivatives exhibit a plateauing behaviour at about 25%. This is broadly consistent with the inversion results shown in Figures 9 and 10. In particular, the crosshole geometry reaches a plateau with fewer data points than the surface geometry. This observation also aligns with the inversion experiments, where satisfactory model reconstruction is achieved with a smaller fraction of data points in the crosshole configuration, reflecting its superior illumination properties. For both geometries, a marked increase in the derivative of the Hessian diagonal is observed between 50 and 75% of included data points. Inspection of the corresponding sensitivity vectors reveals highly localized features that do not align with the expected wave-based illumination patterns at the considered frequency. Owing to their spatial concentration, these components exhibit strong mutual orthogonality, which explains the observed rise in amplitude. However, given their limited physical plausibility and localized character, we exclude them from the selection process.

For comparison, the same analysis is performed for the mean of the random selection strategy. The sum of the Hessian diagonal shows a near linear increase with the number of selected data points. The corresponding derivative remains approximately constant, without any clear plateauing behaviour. This is expected, as the random selection does not prioritize data points based on their information content, leading to a more uniform accumulation of curvature information as more data points are included.

To further assess whether the observed plateau in the Hessian diagonal sum reliably reflects inversion performance, we additionally evaluate an established optimal experimental design (OED) criterion and compute the normalized relative eigenvalue range (nRER), defined as the ratio of the number of eigenvalues exceeding a prescribed threshold (Maurer, Greenhalgh, et al. 2009). For the moderate problem sizes considered here, the eigenvalue decomposition of $\mathbf{J}^\top \mathbf{J}$ can be computed explicitly, allowing direct evaluation of the nRER.

The nRER curves exhibit a plateauing behaviour similar to that observed for the derivative of the Hessian diagonal sum, with stabilization occurring at approximately 50% of the selected data points (Figure 11c). Although the nRER curve is coarsely sampled, this consistency indicates that the growth of the Hessian diagonal sum captures the essential evolution of the information content of the Gauss–Newton system. Consequently, the derivative of the Hessian diagonal sum provides a computationally inexpensive and practical surrogate criterion for determining an appropriate number of data points in future large-scale applications, where explicit eigenvalue decompositions are not feasible.

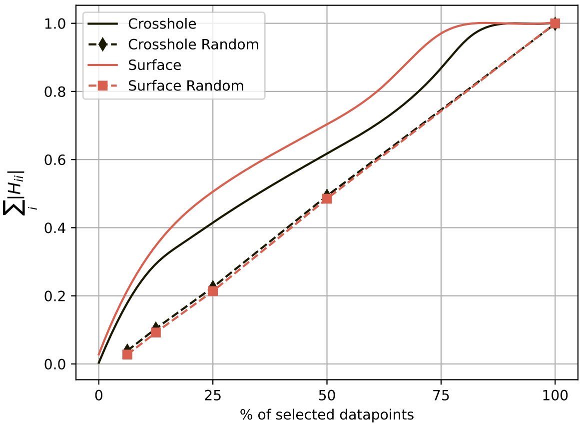

(a) Sum of the diagonal of the approximated Hessian ($\mathbf{J}^\top\mathbf{J}$) as a function of the number of selected data points for both crosshole and surface geometries.

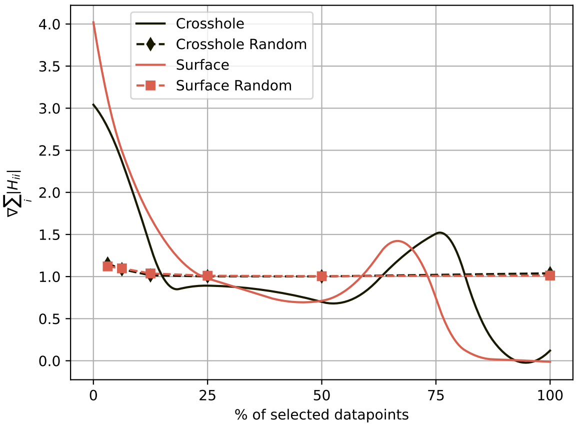

(b) Derivative of the Hessian diagonal sum with respect to the number of selected data points for both crosshole and surface geometries.

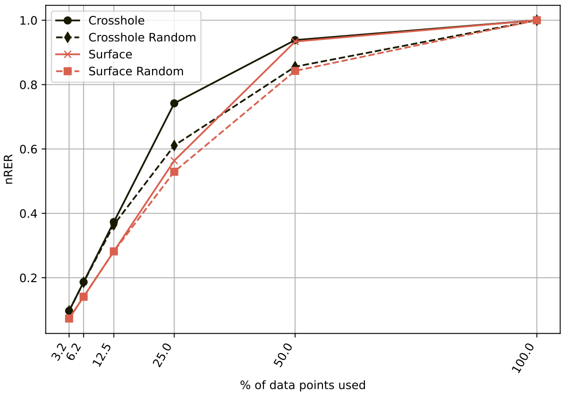

(c) nRER as a function of the number of selected data points for both crosshole and surface geometries.

Figure 11: Comparison of selection criteria for crosshole and surface geometries: (a) sum of Hessian diagonal; (b) derivative of the sum of the diagonal of the Hessian; (c) nRER as a function of the number of selected data points.

4.2 Cost-aware QR Selection

In our time-domain adjoint formulation, the computational cost of assembling a subset of Jacobian rows is determined by the number of distinct forward and adjoint wavefields that must be simulated. Each unique source requires one forward simulation, and each unique receiver requires one adjoint simulation. Consequently, the cost is governed not only by the number of selected source–receiver pairs, but by how these pairs are distributed across sources and receivers. The cost-aware selection strategy penalizes the activation of previously unused sources and receivers, thereby promoting reuse of existing forward and adjoint simulations and reducing the total number of unique simulations required.

The following discussion assumes a fully sampled acquisition geometry in which each source is recorded by all receivers, leading to a complete set of source–receiver pairs. This setting is representative of the synthetic configurations considered in this work and allows for a simple characterization of the relationship between the number of selected pairs and the associated computational cost. Extensions to more irregular acquisition geometries like ocean bottom node surveys or streamer data follow similar principles but lead to less symmetric scaling.

If a fixed number K of pairs is prescribed, from the arithmetic–geometric mean inequality, the minimum cost is obtained when the selected pairs involve approximately $\sqrt{K}$ sources and $\sqrt{K}$ receivers, forming an almost square block of size $\sqrt{K} \times \sqrt{K}$. In this case, the total number of simulations scales as $2\sqrt{K}$. More unbalanced selections, where the pairs are spread over many distinct sources and receivers, require substantially more simulations. For example, selecting 100 source–receiver pairs (25 % of the data) implies a lower bound of 20 simulations, corresponding to $2 \times \sqrt{100}$. The maximum number of simulations needed to reconstruct the full Jacobian is the number of unique sources (20) plus the number of unique receivers (20) which leads to 40 simulations in total.

By introducing the penalty term c in Algorithm 2, we reduce the number of unique simulations to 21 for the crosshole geometry, which is close to this lower bound. For consistency, the same penalty term is applied to the surface geometry. Owing to the markedly different illumination and resolution properties, the minimum number of unique simulations achieved in the surface case is only 29. This reflects the competition in Algorithm 2 between the information content of a candidate block, measured through its residual norm, and the imposed cost penalty.

The evolution of inversion metrics as a function of the fraction of unique simulations is shown in Figure 13 and Figure 14. The black curve represents the nRER metric, which quantifies the information content of the selected data through the eigenvalue spectrum of the Hessian. It is expected to increase as more unique simulations are included, reflecting the accumulation of curvature information. The orange curve corresponds to the relative misfit and should decrease as more unique simulations are incorporated, indicating improved data fit. Due to the nonlinearity of the inverse problem, the relative misfit curves, especially for the surface geometry, are not strictly monotonic. Nevertheless, a general decrease in misfit is observed as the number of unique simulations increases. The yellow curve shows the structural similarity index (SSIM) (Wang et al. 2004) between the inverted model and the comprehensive survey inverted model; it is also expected to increase with the number of unique simulations, reflecting improved structural reconstruction. These expected trends are generally observed, although the curves remain largely flat. This indicates that restricting the number of unique simulations has only a limited impact on inversion quality. The consistent behaviour across the three metrics suggests that the spectral information content, the data fit, and the reconstruction quality are affected comparably by the number of unique simulations.

Qualitatively, inspection of the inversion results in Figures 13 and 14 reveals a slight drop in quality when transitioning from row-wise to cost-aware selection, even when no penalty on the number of unique simulations is applied (first row with $c = 0$ and $N_{\text{simulations}} = 40$). This reflects the intrinsic loss of flexibility associated with grouping rows into blocks rather than selecting individual triplets. Beyond this initial reduction, further decreasing the number of unique simulations only marginally affects the inversion results.

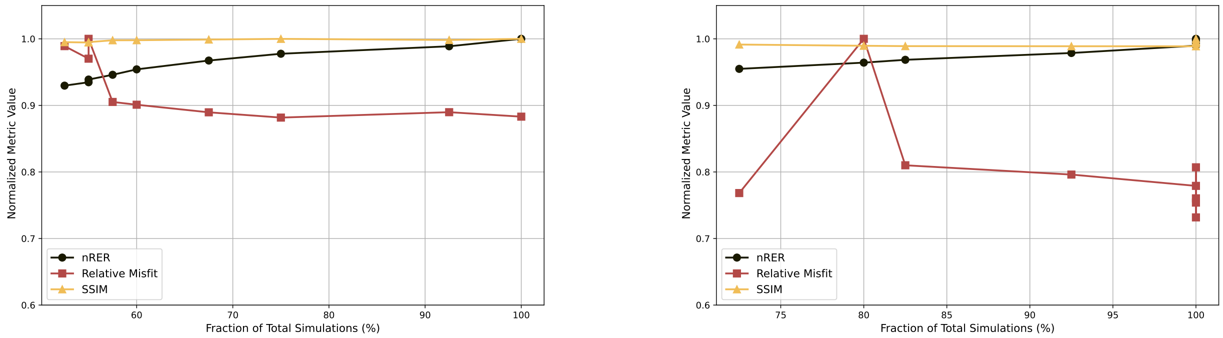

(a) Crosshole geometry

(b) Surface geometry

Figure 12: Normalized inversion performance metrics as a function of unique simulations needed: (a) Crosshole geometry, and (b) Surface geometry.

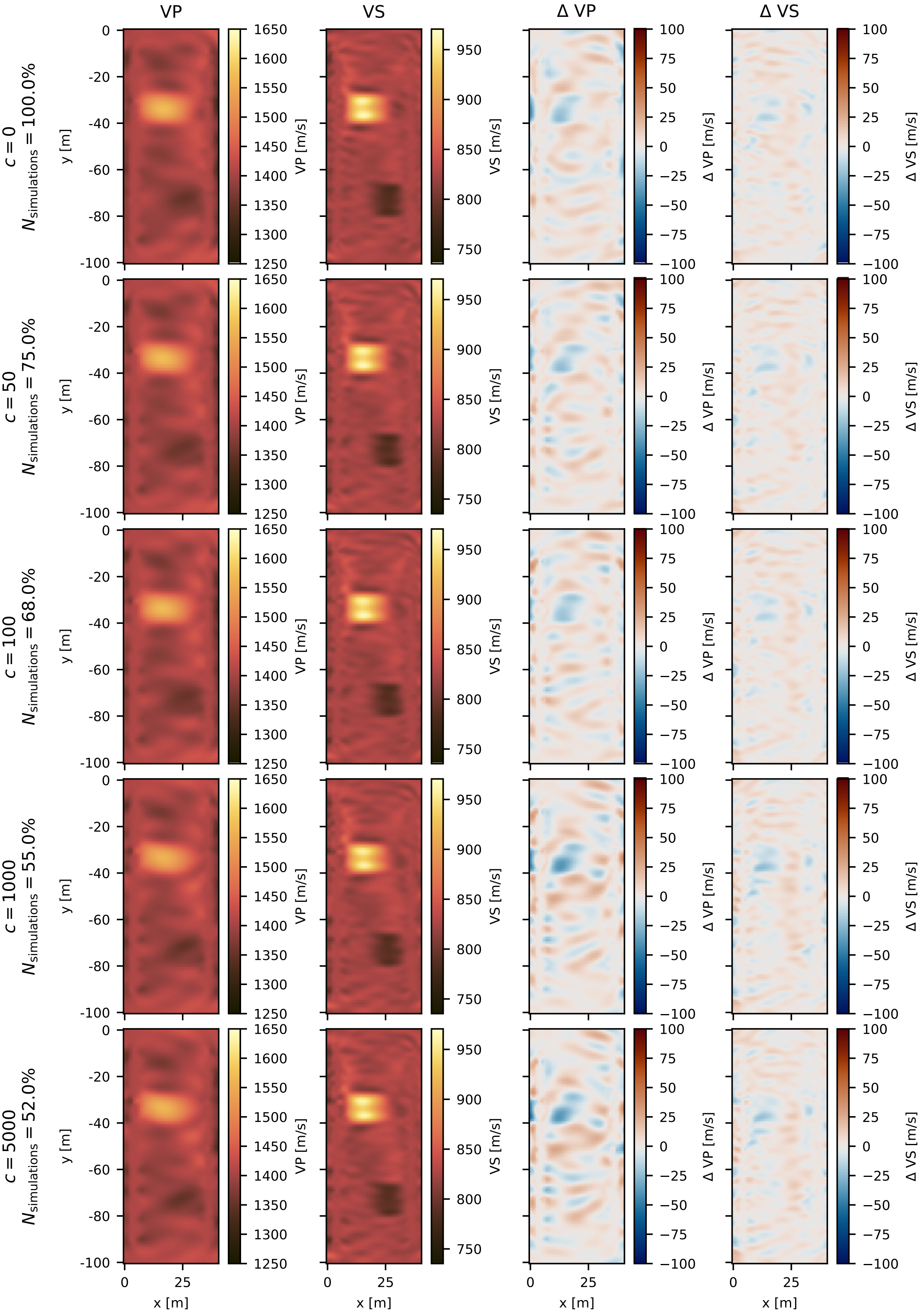

Figure 13: Inversion results for cost-aware selection of 25% of the data with different penalty terms. The model differences are computed with respect to the inverted models not penalized.

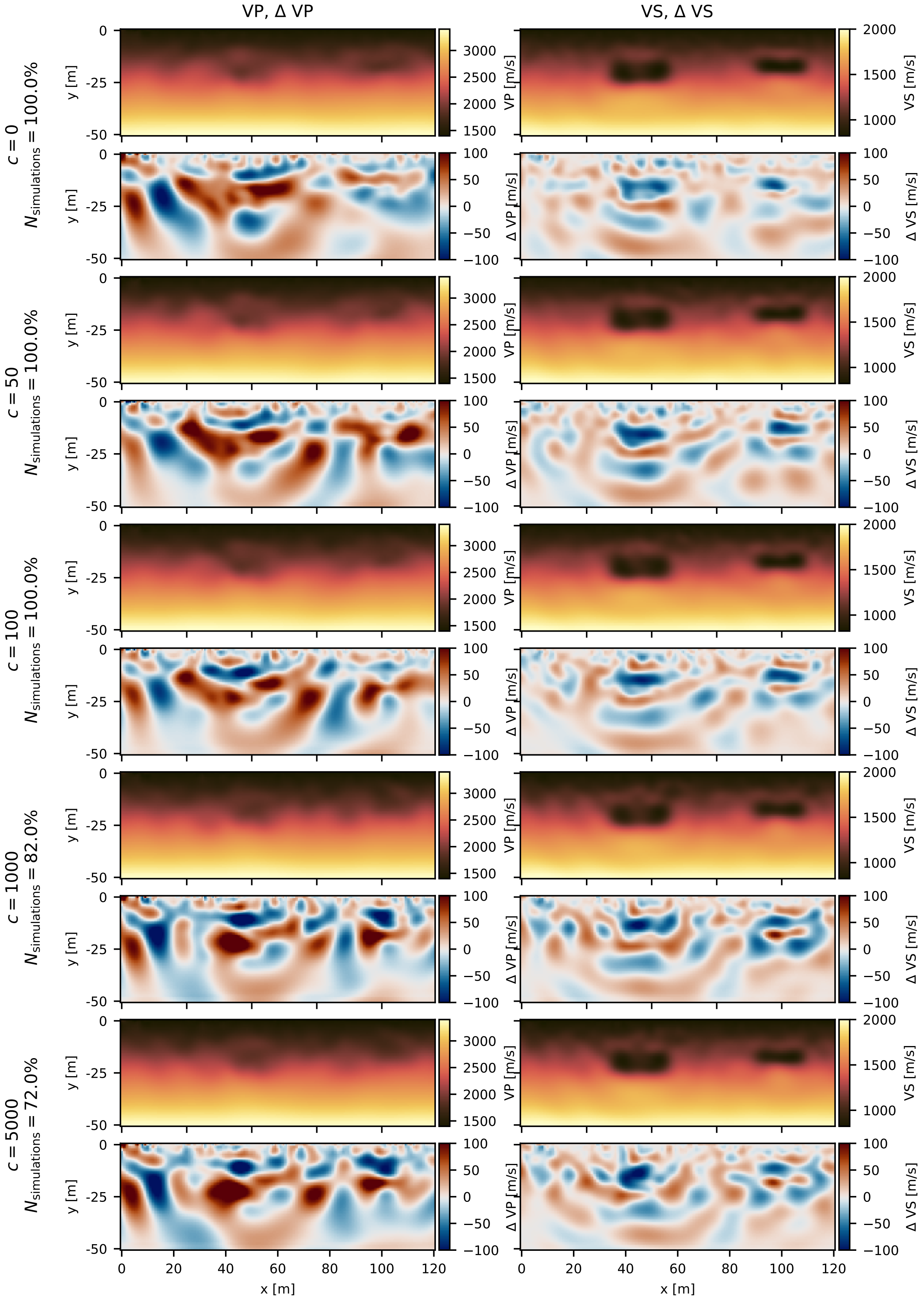

Figure 14: Inversion results for cost-aware selection of 25% of the data with different penalty terms. The model differences are computed with respect to the inverted models not penalized.

4.3 Model compression

In addition to reducing the number of data points, we further decrease the size of the inverse problem by compressing the model space using a wavelet-based representation derived from the Hessian diagonal (Xu et al. 2020; Mercier et al. 2025). The underlying idea is to retain only those wavelet coefficients that account for a prescribed percentage of the cumulative amplitude of the Hessian diagonal, thereby preserving the dominant sensitivity structure while reducing the number of active model parameters.

We apply this model compression in combination with the row-wise selection strategy presented in Section 3.1, as this approach yielded the most compact subsets and the best overall reconstruction quality. For the crosshole geometry, we retain 25% of the data points, while for the surface geometry 50% are selected; both configurations provide satisfactory reconstructions prior to model compression. This ensures that any observed degradation can be attributed to parameter compression rather than insufficient data coverage.

The compression is performed independently for the two model parameters, V_P and V_S, as their sensitivity patterns and compressibility differ significantly. Table 1 summarizes the number of coefficients before and after compression for both parameters and geometries. The corresponding inverted models obtained with and without compression are shown in Figures 15 and 16.

We observe that satisfactory inversion results require retaining 90% of the Hessian diagonal amplitude for the crosshole geometry and 99% for the surface geometry. Two factors may explain this difference. First, the surface configuration uses a larger fraction of data points (50% instead of 25% for the crosshole), which enhances overall illumination and resolution, leading to a richer and less compressible sensitivity structure. Second, the surface geometry is intrinsically more challenging to invert and may therefore be more sensitive to compression-induced artifacts. This behaviour is consistent with the findings of Xu et al. 2020, who also reported reduced compressibility for surface-based acquisition settings.

Case	**Data points included**	**Amplitude retained**	V_P **(before → after)**	V_S **(before → after)**	**Total (before → after)**
Crosshole	25%	90%	4141 → 641	4141 → 1211	8282 → 1852
Surface	50%	99%	4961 → 691	4961 → 1465	9922 → 2156

Table 1: Wavelet-based compression parameter summary for the crosshole and surface cases. Shown are the numbers of coefficients before and after compression for V_P, V_S, and the total, for each geometry.

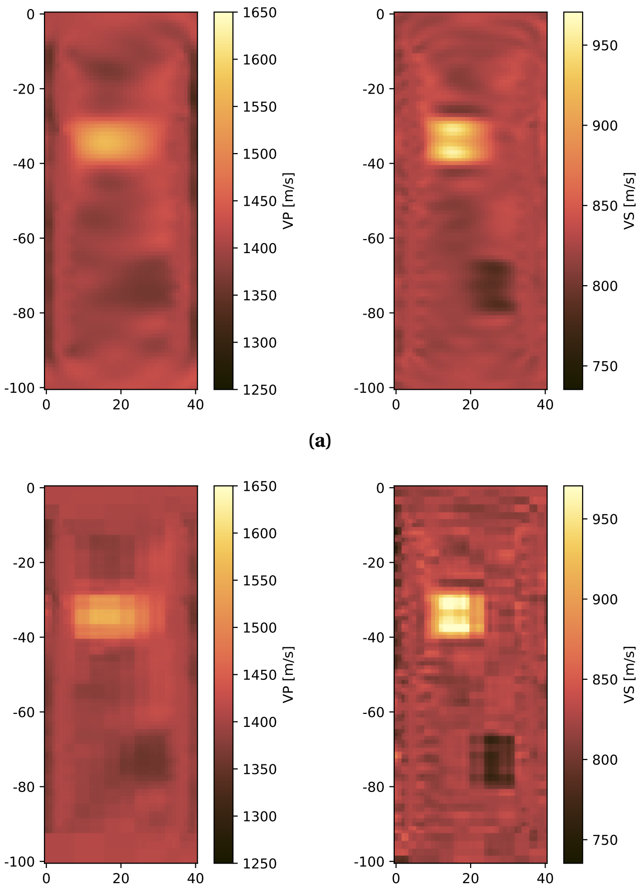

(a)

(b)

Figure 15: Inverted velocity model using 25% of the data with row-wise selection without (a) and with (b) model compression retaining 90% of the amplitude.

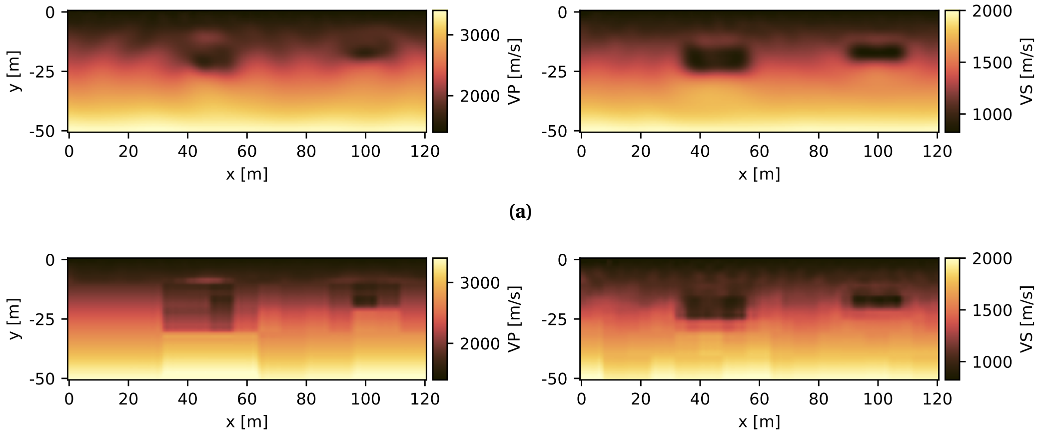

(a)

(b)

Figure 16: Inverted velocity model using 50% of the data with row-wise selection without (a) and with (b) model compression retaining 99% of the amplitude.

4.4 Memory and computation saving

The computational savings achieved by the proposed strategies occur along two independent dimensions: reduction of the size of the Jacobian, through row-wise selection and wavelet-based compression, and reduction of forward and adjoint simulations, through cost-aware selection. To provide a clear comparison, Table 2 reports all costs relative to the comprehensive survey (100%). Jacobian storage and simulation counts are evaluated independently and should not be interpreted as cumulative reductions.

For the crosshole geometry, row-wise selection of 12.5% of the data points reduces the Jacobian, while still delivering satisfactory reconstruction. Applying additional wavelet-based model compression further reduces the effective size to 2.8% of the comprehensive case. For the surface geometry, to reach a comparable satisfactory inversion results, selecting 25% of the data points is required, and subsequent model compression decreases it to approximately 11%. These reductions directly translate into lower memory usage and faster linear-algebra operations in the Gauss–Newton scheme.

In contrast, cost-aware selection primarily targets simulation costs. For the crosshole geometry, the number of unique simulations approaches the theoretical lower bound of 20, leading to a reduction of 53% of required simulations. For the surface geometry, simulation costs can be reduced to 72% of the comprehensive case. These results demonstrate that memory and simulation costs can be controlled independently, depending on the dominant computational bottleneck of the tomographic inversions.

Acq.	**Method**	**Jacobian size (%)**	**Simulations (%)**
Crosshole	Comprehensive	100	100
	Row-wise selection	12.5	100
	+ Wavelet compression	2.8	100
	Cost-aware selection	25	53
Surface	Comprehensive	100	100
	Row-wise selection	25	100
	+ Wavelet compression	10.9	100
	Cost-aware selection	25	72

Table 2: Relative memory and simulation cost with respect to the comprehensive survey (100%). Reductions in Jacobian size and number of simulations are reported independently and are not cumulative.

5 Discussion

Beyond computational savings, the results highlight the role of conditioning in data reduction. QR with pivoting promotes the selection of linearly independent rows and therefore implicitly maximizes the numerical rank of the reduced system. This explains the consistently improved performance relative to random selection, particularly for the more challenging surface geometry. While random subsets may contain redundant or poorly conditioned combinations of sensitivities, QR-based selection preserves the dominant structure of the Gauss–Newton system. The observed plateau behaviour in the Hessian diagonal sum and nRER further supports this interpretation.

In contrast to stochastic subsampling or mini-batching approaches, the present framework is deterministic once the compression operator $\mathbf{\Omega}$ is fixed. Rather than relying on averaging effects across multiple random realizations, it explicitly constructs subsets that approximate the column space of the full Jacobian. This deterministic nature improves reproducibility and reduces variance in inversion outcomes, which may be advantageous in applications, where stability and interpretability are critical.

The numerical experiments illustrate a progressive reduction strategy guided by the dominant computational bottleneck. Row-wise QR selection primarily addresses memory and linear-algebra costs by reducing the number of linearized equations. Cost-aware selection targets the cost of forward and adjoint simulations by explicitly minimizing the number of unique source–receiver simulations. Finally, wavelet-based model compression reduces the number of active model parameters while preserving dominant curvature information. This is also contributing to reduce the amount of memory.

Consequently, any application should begin by identifying the dominant computational bottleneck; whether memory footprint or simulation costs, and selecting the reduction mechanism that addresses it most effectively. In many cases, a combination of these techniques may provide the best trade-off between computational efficiency and imaging quality. The numerical results demonstrate that substantial reductions can be achieved without significant degradation of inversion performance, provided that the reduction strategy is aligned with the structure and illumination characteristics of the acquisition geometry.

The effectiveness of these reductions is strongly dependent on model illumination. The crosshole geometry, characterized by more uniform angular coverage, allows aggressive data and model compression while maintaining inversion quality. In contrast, the surface geometry requires a larger fraction of data points and retains more model coefficients to achieve comparable reconstruction. This confirms that data redundancy and parameter compressibility are intrinsically linked to illumination quality.

The reductions of computational cost obtained through QR-based selection must also be weighted against the additional computational effort required by this method. Constructing the reduced system requires computing QR factorizations of compressed Jacobian representations, which introduces an upfront cost in both memory and computation. If the compressed Jacobian has dimensions $p \times d$ with $p \ll d$, the cost of the pivoted QR factorization scales approximately as

$\mathcal{O}(dp^2)$. This single upfront cost can be higher then solving the Gauss-Newton system via conjugate gradient that scales with $\mathcal{O}(kdp)$, where k is the number of CG iteration required (Golub et al. 1996). However, a single Gauss–Newton iteration requires on the order of $n_s + n_r$ forward and adjoint wavefield simulations, which dominate the computational budget in FWI. Because the QR factorization is performed only once prior to the inversion while the selected data subset is reused across all iterations, even moderate reductions in the number of required simulations is expected to compensate for the initial design cost.

The present experiments consider small sized problems, for which compressed Jacobians can be constructed explicitly and QR factorization obtained in seconds while a single inversion iteration requires multiple minutes. For large-scale three-dimensional surveys, direct QR factorization of the compressed matrices may become infeasible. Potentially, a per shot or per receiver QR factorizations with a weighted combination strategy could be employed similar to the work of Winner et al. 2023. Matrix-free implementations based on Jacobian–vector products represent also possible avenues for scaling to larger problems. Considering the orthogonality of the Jacobian rows to select a subset as suggested by Stummer et al. 2004 provides also a computationally accessible method.

The proposed framework is not restricted to elastic full-waveform inversion. Because the methodology operates purely at the level of the linearized inverse problem, it applies to any gradient-based formulation in which sensitivities or Jacobians can be computed. The selection mechanism acts on algebraic structure rather than on the physics of wave propagation, making it inherently general.

This abstraction enables natural extensions to heterogeneous and mixed datasets. Multi-physics inversion problems, joint inversions, or combinations of acquisition geometries can be treated within a unified selection framework, where sensitivities from different modalities are ranked and selected consistently according to their contribution to conditioning and curvature. Rather than prescribing reduction independently for each data type, the QR-based strategy provides a principled mechanism for identifying the most informative equations across the entire coupled system.

More broadly, the formulation can be interpreted as an algebraic reduction strategy for large-scale PDE-constrained inverse problems. Applications such as travel-time tomography, electromagnetic inversion, ultrasound computed tomography, or structural health monitoring all involve linearized systems in which computational cost is governed by the size and conditioning of the sensitivity matrix. In this sense, the present work establishes a general approach for controlling computational complexity by selecting informative subsets of linearized equations while preserving the essential structure of the inverse problem.

6 Conclusion

In this work, we reformulated post-acquisition data reduction in full-waveform inversion as a matrix row-subset selection problem acting directly on the linearized Gauss–Newton system. By adapting rank-revealing QR factorization to the structure of the Jacobian, we developed two complementary strategies: a row-wise selection method targeting memory and linear-algebra costs, and a cost-aware selection method explicitly reducing the number of unique forward and adjoint simulations. In addition, wavelet-based model compression derived from the Hessian diagonal was shown to further reduce the number of active model parameters.

The numerical experiments demonstrate that substantial reductions in both data volume and model dimension can be achieved while preserving inversion quality. The degree of admissible reduction depends strongly on acquisition geometry and illumination: well-illuminated configurations allow more aggressive compression, whereas poorly illuminated geometries require a larger fraction of data and model coefficients to maintain stability. These results highlight that computational savings should be guided by the dominant bottleneck of the inversion and adapted to the physical structure of the problem.

Importantly, the proposed framework is purely algebraic and does not modify the forward operator or optimization scheme. It therefore provides a flexible post-acquisition strategy that can be integrated into existing Gauss–Newton workflows. While demonstrated here for seismic FWI, the methodology applies more broadly to gradient-based inverse problems in which Jacobians or sensitivity operators are available.

By shifting the perspective from acquisition design to algebraic selection within the linearized system, this work establishes a principled approach for controlling computational complexity in large-scale inverse problems. Future developments will focus on scalable implementations suitable for very large datasets and how this tools can be generalized to different optimization schemes.

References

Abdellaziz, Amine, Romain Brossier, Ludovic Métivier, and Édouard Oudet (Jan. 7, 2025). “Optimal experimental design for full waveform inversion using a wavenumber sampling criterion—part 1 : 2-D to methodological development”. en. In: *Geophysical journal international* 240 (3), pp. 1429–1459. ISSN: 1365-246X,0956-540X. DOI: 10.1093/gji/ggae454.

Afanasiev, Michael, Christian Boehm, Martin van Driel, Lion Krischer, Max Rietmann, Dave A May, Matthew G Knepley, and Andreas Fichtner (Mar. 1, 2019). “Modular and flexible spectral-element waveform modelling in two and three dimensions”. en. In: *Geophysical Journal International* 216 (3), pp. 1675–1692. ISSN: 0956-540X,1365-246X. DOI: 10.1093/gji/ggy469.

Businger, Peter and Gene H Golub (June 1965). “Linear least squares solutions by householder transformations”. en. In: *Numerische mathematik* 7 (3), pp. 269–276. ISSN: 0029-599X,0945-3245. DOI: 10.1007/bf01436084.

Castellanos, Clara, Ludovic Métivier, Stéphane Operto, Romain Brossier, and Jean Virieux (Feb. 1, 2015). “Fast full waveform inversion with source encoding and second-order optimization methods”. en. In: *Geophysical Journal International* 200 (2), pp. 720–744. ISSN: 0956-540X,1365-246X. DOI: 10.1093/gji/ggu427.

Clark, Emily, Steven L Brunton, Senior Member, J Nathan Kutz, and Member (2020). “Multi-fidelity sensor selection: Greedy algorithms to place cheap and expensive sensors with cost constraints”. In.

Curtis, Andrew (Oct. 1, 1999). “Optimal design of focused experiments and surveys”. en. In: *Geophysical Journal International* 139 (1), pp. 205–215. ISSN: 0956-540X. DOI: 10.1046/j.1365-246X.1999.00947.x.

Drmač, Zlatko and Serkan Gugercin (Jan. 1, 2016). “A new selection operator for the discrete empirical interpolation method—improved A Priori error bound and extensions”. en. In: *SIAM journal on scientific computing: a publication of the Society for Industrial and Applied Mathematics* 38 (2), A631–A648. ISSN: 1064-8275,1095-7197. DOI: 10.1137/15m1019271.

Duersch, Jed A and Ming Gu (Jan. 1, 2017). “Randomized QR with column pivoting”. en. In: *SIAM journal on scientific computing: a publication of the Society for Industrial and Applied Mathematics* 39 (4), pp. C263–C291. ISSN: 1064-8275,1095-7197. DOI: 10.1137/15m1044680.

Eswar, Srinivas, Vishwas Rao, and Arvind K Saibaba (Feb. 25, 2024). “Bayesian D-optimal experimental designs via column subset selection”. In: *arXiv [math.NA]*. arXiv: 2402.16000 [math.NA].

Fichtner, Andreas (Nov. 23, 2010). *Full seismic waveform modelling and inversion*. en. 2011th ed. Advances in geophysical and environmental mechanics and mathematics. Berlin, Germany: Springer. 343 pp. ISBN: 9783642158063,9783642158070. DOI: 10.1007/978-3-642-15807-0.

Golub, Gene H and Charles F Van Loan (Oct. 11, 1996). *Matrix Computations*. en. 3rd ed. Johns Hopkins Series in the Mathematical Sciences. Baltimore, MD: Johns Hopkins University Press. 728 pp. ISBN: 9780801854149.

Gu, Ming and Stanley C Eisenstat (July 1996). “Efficient algorithms for computing a strong rank-revealing QR factorization”. en. In: *SIAM journal on scientific computing: a publication of the Society for Industrial and Applied Mathematics* 17 (4), pp. 848–869. ISSN: 1064-8275,1095-7197. DOI: 10.1137/0917055.

Halko, N, P G Martinsson, and J A Tropp (Jan. 5, 2011). “Finding structure with randomness: Probabilistic algorithms for constructing approximate matrix decompositions”. en. In: *SIAM review. Society for Industrial and Applied Mathematics* 53 (2), pp. 217–288. ISSN: 0036-1445,1095-7200. DOI: 10.1137/090771806.

Herrmann, Felix J, Ian Hanlon, Rajiv Kumar, Tristan van Leeuwen, Xiang Li, Brendan Smithyman, Haneet Wason, Andrew J Calvert, Mostafa Javanmehri, and Eric Takam Takougang (Sept. 2013). “Frugal full-waveform inversion: From theory to a practical algorithm”. en. In: *Leading Edge* 32 (9), pp. 1082–1092. ISSN: 1070-485X,1938-3789. DOI: 10.1190/tle32091082.1.

Herwaarden, Dirk Philip van, Christian Boehm, Michael Afanasiev, Solvi Thrastarson, Lion Krischer, Jeannot Trampert, and Andreas Fichtner (May 1, 2020). “Accelerated full-waveform inversion using dynamic mini-batches”. en. In: *Geophysical journal international* 221 (2), pp. 1427–1438. ISSN: 0956-540X,1365-246X. DOI: 10.1093/gji/ggaa079.

Krampe, Valérie, Pascal Edme, and Hansruedi Maurer (Jan. 2021). “Optimized experimental design for seismic full waveform inversion: A computationally efficient method including a flexible implementation of acquisition costs”. en. In: *Geophysical Prospecting* 69 (1), pp. 152–166. ISSN: 0016-8025,1365-2478. DOI: 10.1111/1365-2478.13040.

Krebs, Jerome R, John E Anderson, David Hinkley, Ramesh Neelamani, Sunwoong Lee, Anatoly Baumstein, and Martin-Daniel Lacasse (Jan. 1, 2009). “Fast full-wavefield seismic inversion using encoded sources”. en. In: *Geophysics* 74 (6), WCC177–WCC188. ISSN: 0016-8033,1942-2156. DOI: 10.1190/1.3230502.

Li, Xiang, Aleksandr Y Aravkin, Tristan van Leeuwen, and Felix J Herrmann (May 1, 2012). “Fast randomized full-waveform inversion with compressive sensing”. en. In: *Geophysics* 77 (3), A13–A17. ISSN: 0016-8033,1942-2156. DOI: 10.1190/geo2011-0410.1.

Manohar, Krithika, Bingni W Brunton, J Nathan Kutz, and Steven L Brunton (June 2018). “Data-driven sparse sensor placement for reconstruction: Demonstrating the benefits of exploiting known patterns”. en. In: *IEEE control systems* 38 (3), pp. 63–86. ISSN: 1066-033X,1941-000X. DOI: 10.1109/mcs.2018.2810460.

Maurer, Hansruedi, Stewart Greenhalgh, and Sabine Latzel (Nov. 2009). “Frequency and spatial sampling strategies for crosshole seismic waveform spectral inversion experiments”. en. In: *Geophysics* 74 (6), WCC79–WCC89. ISSN: 0016-8033,1942-2156. DOI: 10.1190/1.3157252.

Maurer, Hansruedi, André Nuber, Naiara Korta Martiartu, Fabienne Reiser, Christian Boehm, Edgar Manukyan, Cédric Schmelzbach, and Andreas Fichtner (2017). “Optimized experimental design in the context of seismic full waveform inversion and seismic waveform imaging”. In: *Advances in Geophysics*. Vol. 58. Advances in geophysics. Elsevier, pp. 1–45. ISBN: 9780128124130. DOI: 10.1016/bs.agph.2017.10.001.

Mercier, Arnaud, Christian Boehm, and Hansruedi Maurer (Apr. 8, 2025). “Designing full waveform inverse problems: a combined data and model approach”. en. In: *Geophysical Journal International* 241 (3), pp. 1479–1494. ISSN: 0956-540X,1365-246X. DOI: 10.1093/gji/ggaf117.

Murray, Riley et al. (Feb. 22, 2023). “Randomized numerical linear algebra : A perspective on the field with an eye to software”. In: *arXiv [math.NA]*. DOI: 10.48550/arXiv.2302.11474. arXiv: 2302.11474 [math.NA].

Nuber, André, Edgar Manukyan, and Hansruedi Maurer (Sept. 20, 2017). “Optimizing measurement geometry for seismic near-surface full waveform inversion”. en. In: *Geophysical journal international* 210 (3), pp. 1909–1921. ISSN: 0956-540X,1365-246X. DOI: `10.1093/gji/ggx267`.

Pratt, Gerhard, Changsoo Shin, and Hicks (May 26, 1998). “Gauss-Newton and full Newton methods in frequency-space seismic waveform inversion”. en. In: *Geophysical journal international* 133 (2), pp. 341–362. ISSN: 0956-540X,1365-246X. DOI: `10.1046/j.1365-246x.1998.00498.x`.

Stummer, Peter, Hansruedi Maurer, and Alan G Green (Jan. 2004). “Experimental design: Electrical resistivity data sets that provide optimum subsurface information”. en. In: *Geophysics* 69 (1), pp. 120–139. ISSN: 0016-8033,1942-2156. DOI: `10.1190/1.1649381`.

Tarantola, Albert (Jan. 2005). *Inverse problem theory and methods for model parameter estimation*. Society for Industrial and Applied Mathematics. ISBN: 9780898715729,9780898717921. DOI: `10.1137/1.9780898717921`.

Virieux, J and S Operto (Nov. 1, 2009). “An overview of full-waveform inversion in exploration geophysics”. en. In: *Geophysics* 74 (6), WCC1–WCC26. ISSN: 0016-8033,1942-2156. DOI: `10.1190/1.3238367`.

Wang, Zhou, Alan Conrad Bovik, Hamid Rahim Sheikh, and Eero P Simoncelli (Apr. 2004). “Image quality assessment: from error visibility to structural similarity”. en. In: *IEEE Transactions on Image Processing* 13 (4), pp. 600–612. ISSN: 1057-7149,1941-0042. DOI: `10.1109/tip.2003.819861`.

Winner, Valérie, Pascal Edme, and Hansruedi Maurer (Jan. 2023). “Model-based optimization of source locations for 3D acoustic seismic full-waveform inversion”. en. In: *Geophysical Prospecting* 71 (1), pp. 3–16. ISSN: 0016-8025,1365-2478. DOI: `10.1111/1365-2478.13264`.

Witte, Philipp A, Mathias Louboutin, Fabio Luporini, Gerard J Gorman, and Felix J Herrmann (Sept. 1, 2019). “Compressive least-squares migration with on-the-fly Fourier transforms”. en. In: *Geophysics* 84 (5), R655–R672. ISSN: 0016-8033,1942-2156. DOI: `10.1190/geo2018-0490.1`.

Xu, Linan, Edgar Manukyan, and Hansruedi Maurer (Apr. 13, 2020). “Optimized model parameterization using Compact Full Waveform Inversion”. en. In: *Geophysical Journal International*. ISSN: 0956-540X,1365-246X. DOI: `10.1093/gji/ggaa175`.

Zhou, Bing and Stewart Greenhalgh (Sept. 2009). “On the computation of the Fréchet derivatives for seismic waveform inversion in 3D general anisotropic, heterogeneous media”. en. In: *Geophysics* 74 (5), WB153–WB163. ISSN: 0016-8033,1942-2156. DOI: `10.1190/1.3123766`.

A Appendix

A.1 Inversion results of the closest to mean random selection

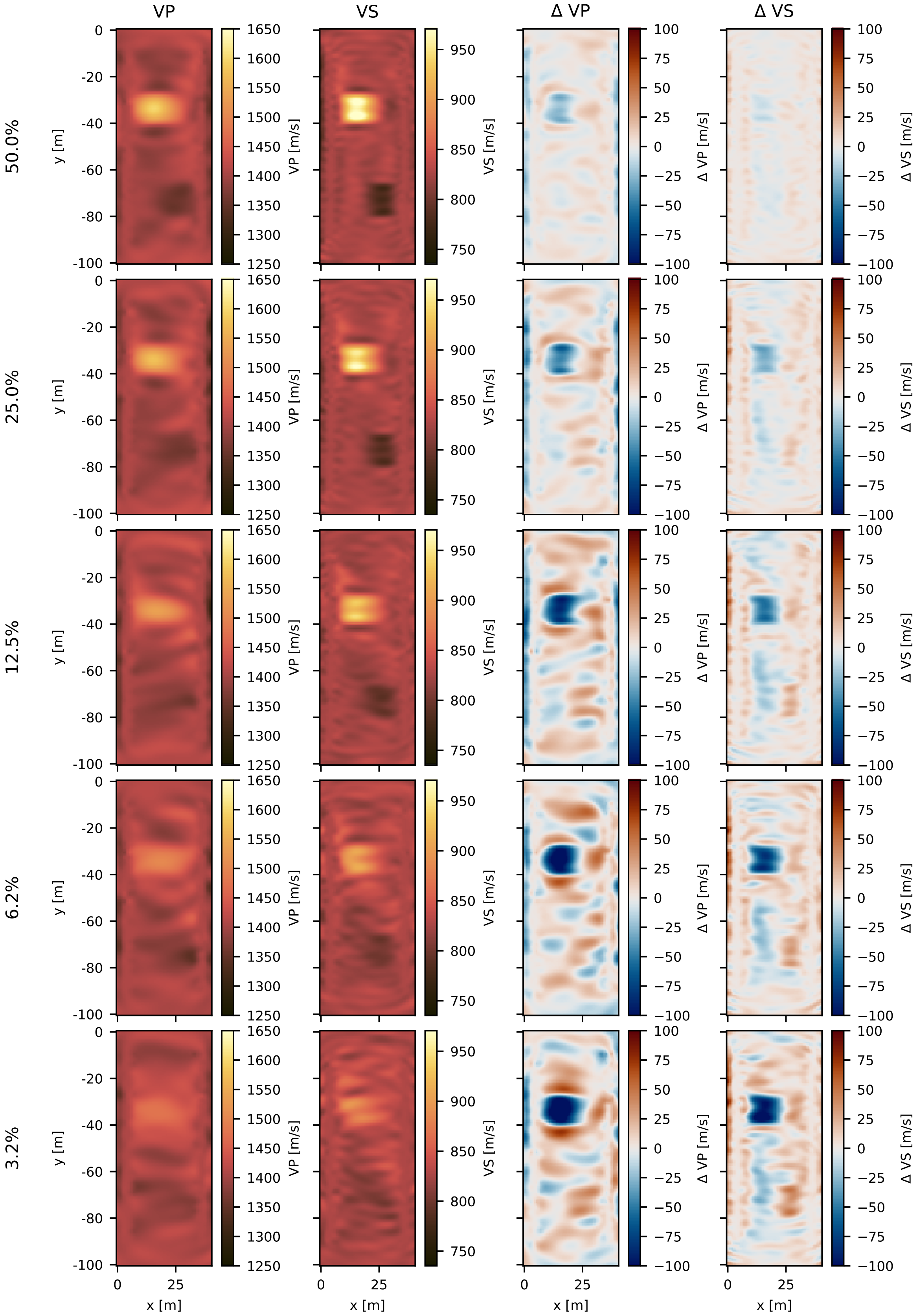

Figure 17: Inverted models of the crosshole geometry for the random selection closest to the mean result for different number of data points accompanied by their differences with respect to the inverted models with the comprehensive survey.

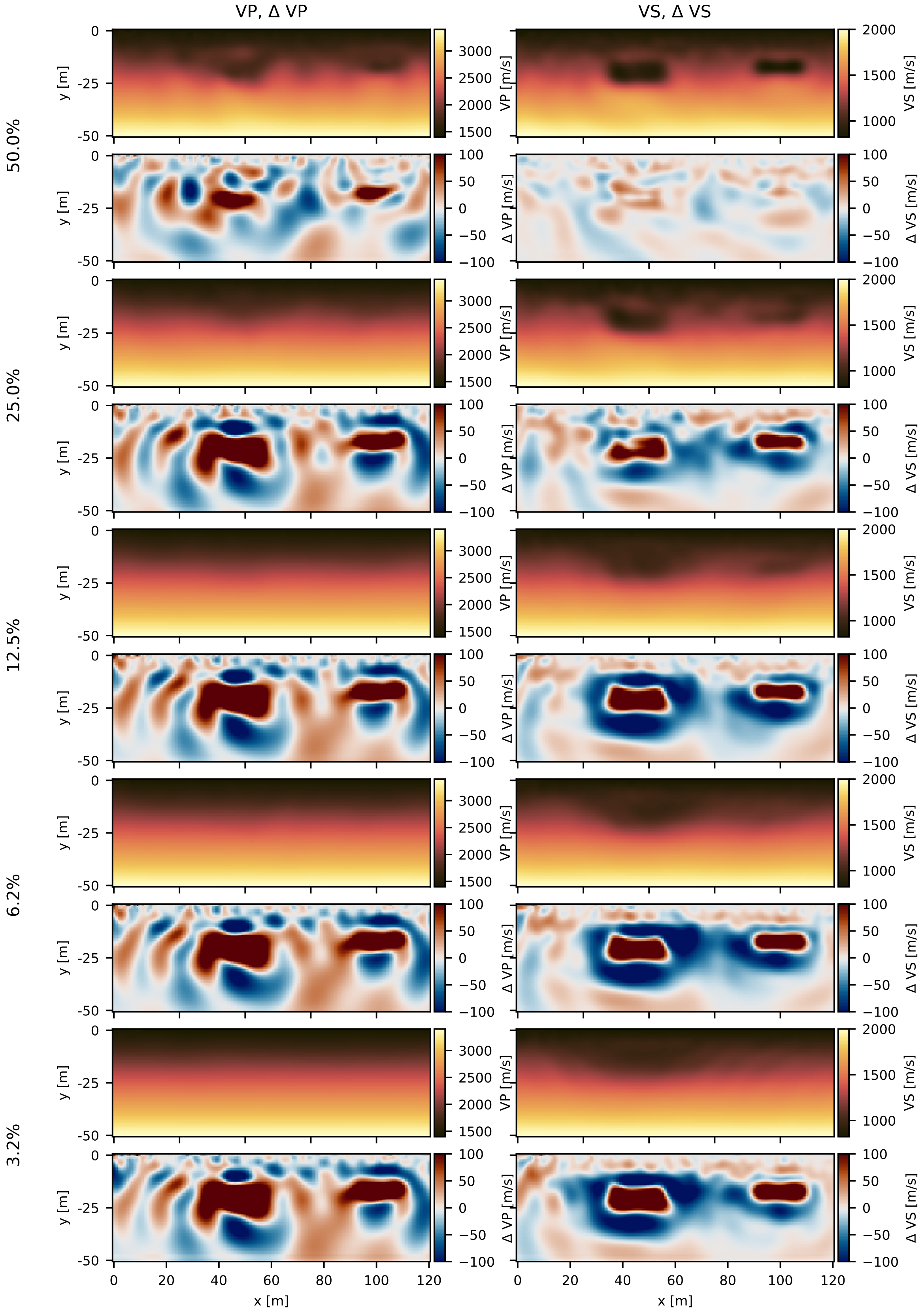

Figure 18: Inverted models of the surface geometry for the random selection closest to the mean result for different number of data points accompanied by their differences with respect to the inverted models with the comprehensive survey.